THE JOURNAL OF
PHYSICAL CHEMISTRY C

ARTICLE

pubs.acs.org/JPCC

Nanostructure Development in Alkoxide-Carboxylate-Derived Precursor Films of Barium Titanate

Tomasz M. Stawski,[†] Sjoerd A. Veldhuis,[†] Rogier Besselink,[†] Hessel L. Castricum,[‡] Giuseppe Portale,[§]
Dave H. A. Blank,[†] and Johan E. ten Elshof[*,†]

[†]MESA[+] Institute for Nanotechnology, University of Twente, P.O. Box 217, 7500 AE Enschede, The Netherlands
[‡]Van't Hoff Institute for Molecular Sciences, University of Amsterdam, Science Park 904, 1098 XH Amsterdam, The Netherlands
[§]Netherlands Organization for Scientific Research, DUBBLE@ESRF, BP 220, Grenoble F38043, France

ABSTRACT: The structural evolution in wet alkoxide-carboxylate sol−gel precursor films of barium titanate upon drying was investigated by time-resolved small-angle X-ray scattering (SAXS). The morphology of as-dried amorphous precursor thin films was investigated by transmission electron microscopy (TEM) and electron energy loss spectroscopy (EELS). Sols were prepared from titanium(IV) *iso*-propoxide in 2-methoxyethanol and barium acetate in acetic acid. The structures that were visible with SAXS could be divided into oligomeric structures with fractal-like scattering characteristics, and randomly packed agglomerates of nanoparticles of similar size. The fractal-like morphologies disappeared during film drying, probably because they were not stable in the absence of a solvent matrix. Only the ordered agglomerate-like structures remained in the as-dried films. EELS on as-dried films showed that spatial separation between barium and titanium-rich domains occurred during the drying of the thin films on a length scale of nanometers, depending on hydrolysis ratio. This demonstrates that as-dried films are not necessarily uniform on the mesoscopic level.

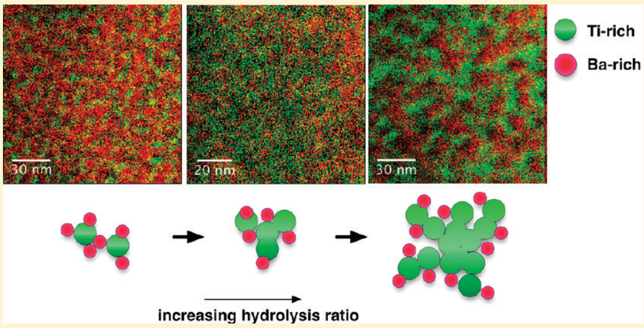

1. INTRODUCTION

Barium titanate ($BaTiO_3$) is a high-*k* dielectric material used in commercial multilayer ceramic capacitors. The minimum $BaTiO_3$ layer thickness that can be achieved with state of the art tape casting methods is about 1 μm. Barium titanate is used in crystalline form, which implies the use of starting powders with a particle size of ca. 200 nm.[1] Further reduction of the barium titanate layer thickness requires finer powders obtained by new synthesis and deposition techniques. One of the feasible alternatives is the deposition of amorphous precursors of barium titanate and their further reaction and crystallization to a perovskite phase.[2] Good control and understanding of the process in all stages is required to obtain a film with the desired electrical and morphological properties. This can be achieved by wet-chemical processing methods.

Wet-chemical methods provide nanometer-sized powders (5−100 nm) of high purity and homogeneity, and of adjustable composition, as near-atomic level mixing of components is possible.[3] Among these methods the sol−gel process, in particular the alkoxide-carboxylate synthesis, the double alkoxide synthesis, the microemulsion synthesis, and the precipitation methods (alkoxide-hydroxide sol precipitation) have received much attention.[3] As the sol−gel process is based on liquid precursors, direct deposition of precursor thin films onto substrates by means of spin-casting, deep-casting, or misted source deposition, followed by pyrolysis and crystallization is possible.[2,4,5] The alkoxide-carboxylate route has been employed widely for $BaTiO_3$ synthesis since the first reports.[6] Barium titanate xerogels were synthesized from titanium(IV) *iso*-propoxide in *iso*-propanol and barium acetate dissolved in acetic acid. Acetic acid was used as a solvent enabling the complete dissolution of barium acetate. Acetic acid is also known to chelate metal centers in alkoxides, leading to the formation of oligomeric metal oxoacetates.[3,4,7] Therefore the alkoxide-carboxylate process is often referred to as a hybrid process, because it combines a classical sol−gel precursor (metal alkoxide) with a non-sol−gel precursor (metal carboxylate).[2,4]

The influence of precursor chemistry and processing conditions on the morphology of crystalline thin films processed from the hybrid process was investigated.[8,9] Use of acetic acid or propionic acid favored the growth or larger grains and yielded higher density films in comparison with films synthesized from longer carboxylic acid based precursors. The difference was attributed to the higher pyrolysis temperature of the system containing the shorter carboxylic acid, which led to the formation of the transition oxocarbonate phase $Ba_2Ti_2O_5CO_2$.[3,10] Crystallization occurred at higher temperatures, which led to increased film density and larger grains. The morphology of crystalline (Ba,Sr)TiO_3 and $BaTiO_3$ films derived from the alkoxide-carboxylate route could be also modified.[9] When the sol concentration was

Received: October 5, 2011
Revised: December 5, 2011
Published: December 06, 2011

sufficiently low, columnar grains formed, provided that the films were deposited in a number of steps and crystallized after each deposition step. Above a certain threshold concentration a granular morphology was observed. The stabilization of titanium alkoxide precursors is believed to play an important role here, as it can modify the hydrolysis and condensation pathways. For instance, stabilization of titanium alkoxide with acetylacetone resulted in denser films with larger grain sizes and better dielectric properties.[2,8] This was attributed to the monomeric character of the titanium precursor and the homogeneous mixing of Ti and Ba precursors on the nanometer scale. It was hypothesized that in the case of nonstabilized solutions, an oligomeric TiO_x phase might form, and the extent of phase formation would depend on the extent of Ti alkoxide oligomerization. The structure of such an alkoxide-carboxylate gel was proposed by Hennings et al.,[11] based on transmission electron microscopy (TEM), energy dispersive spectroscopy (EDS), and infrared spectroscopy (FT-IR) analysis. Metal carboxylate species were assumed to adsorb on the surface of the titanium oxoacetate polymer. The separation between Ti-rich and Ba-rich regions exceeded 100 nm.

Relatively few details are known on the kinetics and morphology of barium titanate alkoxide-carboxylate precursors upon reaction and physical drying. So far, pioneering SAXS studies of analogous alkoxide-carboxylate lead zirconate titanate precursor sols were conducted by Zhang et al.[12−14] However, the precursor solutions of barium titanate and lead zirconate titanate are not structurally similar.[15,16] In a previous study on barium titanate solutions we reported the structural evolution of hydrolyzed sols by small-angle X-ray scattering (SAXS) and viscosity measurements.[16] The results suggested that both fractal-like and agglomerate-like structures were present in solution. The primary scatterers from which these structures were formed were Ti-based, and consisted of small spherical primary particles of very similar size. The majority species after reaction in constant volume were fractal-like structures.

However, for sol−gel processing of thin films the drying stage of the sol is also very interesting. Due to the fact that volatile components of the system evaporate, the actual precursor concentration increases rapidly, yielding fast sol−gel transitions in the final stages of physical drying. It was the aim of this work to monitor the structural evolution in wet thin films from model solutions of titanium alkoxide and barium acetate in acetic acid during the drying process. We employed time-resolved small-angle X-ray scattering (SAXS) to study the structural characteristics of drying films. We used transmission electron microscopy (TEM), and electron energy loss spectroscopy (EELS) for the characterization of as-deposited precursor films.

2. EXPERIMENTAL SECTION

2.1. Synthesis of Barium Titanate (BTO) Precursor Sols.

Barium acetate (>99%, Riedel-deHaën) and titanium(IV) *iso*-propoxide (99.999%, Sigma-Aldrich) were used as precursor materials. Glacial acetic acid (99.8%, Acros) and 2-methoxyethanol (>99.3%, Sigma-Aldrich) were used as solvents, stabilizers, and chelating agents. Two stock solutions were made. A Ba-acetate solution was prepared by dissolving barium acetate in acetic acid and subsequent refluxing at 105 °C for 8 h. The final concentration was adjusted to 1.0 mol/dm^3. The second stock solution was based on titanium *iso*-propoxide with 2-methoxyethanol as solvent yielding a precursor of 1.0 mol/dm^3. It was stirred in a glovebox under nitrogen atmosphere. Both stock solutions were stirred at room temperature for 24 h. They were then stored at room temperature. Prior to the experiments, the stock solutions were mixed in 1:1 molar ratios and stirred for 5 min, yielding a concentration of 0.50 mol/dm^3 in the final BTO precursor solution. Solutions of this concentration were used in all experiments. Hydrolysis was initiated by addition of water immediately after the two stock solutions had been mixed and stirred. The hydrolysis ratio h was defined as

$$h = [H_2O]/[Ti] \quad (1)$$

2.2. Transmission Electron Microscopy (TEM) and Electron Energy Loss Spectroscopy (EELS).

BTO precursor sols with h = 0.0, 2.8, 5.6, and 33, respectively, were spin-casted (Laurell WS-400B-6NPP-Lite spincoater) onto holey carbon TEM copper grids (CF200-Cu, Electron Microscopy Sciences) at 4000 rpm for 40 s. The as-prepared films were dried at 60 °C for 1 h on a hot-stage and used for transmission electron microscopy (TEM) characterization (Philips CM300ST-FEG at 300 kV).

Features of interest were examined at high magnification (GATAN 2k x 2k Ultrascan1000 CCD camera). Energy filtered images (GATAN model Tridiem with 2k x 2k CCD camera) were recorded at the highest possible magnification that still provided stable images, with negligible or compensable drift using the 3-windows method for Ba-$M_{4,5}$ (pre-edge 716 eV, postedge 801 eV, slit width 40 eV, 10 s exposure) and Ti-$L_{2,3}$ (pre-edge 406 eV, postedge 481 eV, slit width 30 eV, 10 s exposure). Color mix maps juxtapositioning selected combinations of elements were manually corrected for drift depending on the element, using the microscope GMS software package.

2.3. Time-Resolved Small Angle X-ray Scattering (SAXS) of Drying BTO Films.

The elastically scattered X-rays by a sample that has local electronic density fluctuations was recorded at small angles.[17−20] The scattering intensity $I(q)$ was recorded versus the scattering vector q (nm^{-1}), which is related to the scattering angle 2θ and the wavelength λ (nm) of the incident beam via

$$q = 4\pi/\lambda \sin \theta \quad (2)$$

SAXS experiments were performed on the Dutch-Belgian beamline (DUBBLE) BM-26B of the ESRF in Grenoble, France.[21] The beam was focused at the corner of a 2D gas-filled multiwire detector in order to maximize the range of accessible q values (scattering vector values). The beam energy was 16 keV (λ = 0.0776 nm). The samples were placed at a distance of 1.5 m away from the detector. Structural information on particles with dimensions up to 50 nm can be derived from the investigated angular range, $0.13 < q < 9.00$ nm^{-1}.[17−20] The raw data were corrected for the pixel-dependent detector sensitivity and integrated for channels with the same q values using a matlab/fit2d routine available at BM-26B.

The setup that was used to follow the evolution of drying thin films is schematically illustrated in Figure 1. BTO sols were contained in a Kapton foil that was mounted on an aluminum rotor head with a diameter of *ca.* 11 cm. The rotation speed was 100 rpm, ensuring a homogeneous distribution of liquid film over the surface of the Kapton foil. The rotation axis was not completely perpendicular to the incoming X-ray beam, as illustrated in Figure 1. This allowed detection of the scattered X-ray beam. Time-resolved SAXS patterns of drying BTO thin films with hydrolysis ratio h = 0.0, 5.6, and 33.0 were recorded at 60 °C over

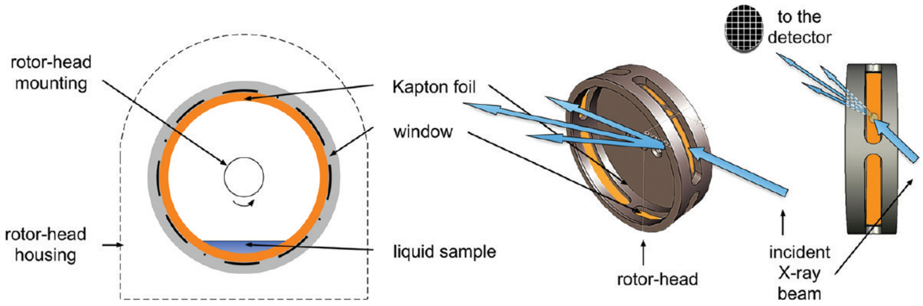

Figure 1. Schematic of the setup used for in situ X-ray scattering measurements of drying thin BTO precursor films.

a period up to 60 min. The scattering intensity of the empty chamber background, i.e. Kapton foil under the same conditions, was subtracted in order to achieve the background correction.

2.4. Crystalline Thin Films and Characterization. BTO precursor sols with $h = 0.0$, 5.6, and 33, respectively, were spin-casted (Laurell WS-400B-6NPP-Lite spincoater) onto Si/Ti/Pt substrates at 2500 rpm for 40 s. The as-prepared films were dried on a hot-stage at 60 °C for 180 min. In subsequent steps, substrates with BTO films were placed in a preheated oven (Milestone PyroPrep) at 700 °C for 15 min, then quenched to room temperature. The Si/Ti/Pt substrates were made by sputtering (Sputterke, DC sputter system, $p_{\mathrm{Ar}} = 0.0066$ mbar, $T = 25$ °C). Si(001) substrates with native SiO_2, a Ti adhesion layer of 25 nm thickness, and a 200 nm thick Pt electrode were used. The samples were broken with pliers and the cross-section was analyzed by Field Emission-Scanning Electron Microscopy (FE-SEM, 0.5 - 2.0 keV, Zeiss 1550) to determine layer thickness and film microstructure. In all the investigated cases phase pure $BaTiO_3$ films were obtained as confirmed by the X-ray powder diffraction (Philips PW1830).

3. SMALL ANGLE X-RAY SCATTERING DATA INTERPRETATION

In our previous study on similar sol−gel barium titanate precursor solutions,[16] we developed a scattering model to describe the precursor solution in terms of a mixture of mass-fractal-like oligomeric structures, and structures with internal correlations, i.e. agglomerates of similarly sized scatterers. Both structures are composed of the same type of spherical scatterers with radius r_0 and form factor $P(q)$.

The fractal-like branched oligomeric or polymeric structures were described using the structure factor $S_{\mathrm{F}}(q)$,[22−24] defined as

$$S_{\mathrm{F}}(q) = 1 + \frac{D\Gamma(D-1)\sin[(D-1)\arctan(q\xi)]}{(qr_0)^D\left[1+\frac{1}{(q^2\xi^2)}\right]^{(D-1)/2}} \tag{3}$$

The parameter D is a fit parameter that relates the mass of agglomerate, i.e., number of particles, to its radius of gyration R_g. The parameter r_0 is the radius of the primary scatterer.

The parameter ξ is a characteristic length scale above which the mass distribution in the structure is no longer fractal-like.[16] Eq 3 is valid when $r_0 \ll \xi$. The radius of gyration of fractal agglomerate, R_g, is then expressed in terms of these parameters as[22−24]

$$R_g^{\,2} = D(D+1)\xi^2/2 \tag{4}$$

The second type of entities in solution are agglomerates of scatterers with similar size. They can be described by the Percus−Yevick structure factor $S_{\mathrm{C}}(q)$[25−28]

$$S_{\mathrm{C}}(q) = \frac{1}{1 + 24\nu G(2qR_{\mathrm{HS}})/(2qR_{\mathrm{HS}})} \tag{5}$$

where

$$\begin{aligned}G(2qR_{\mathrm{HS}}) = {} & \alpha[\sin(2qR_{\mathrm{HS}}) - (2qR_{\mathrm{HS}})\cos(2qR_{\mathrm{HS}})](2qR_{\mathrm{HS}})^{-2}\\ & + \beta[2(2qR_{\mathrm{HS}})\sin(2qR_{\mathrm{HS}})\\ & + (2-(2qR_{\mathrm{HS}})^2)\cos(2qR_{\mathrm{HS}}) - 2](2qR_{\mathrm{HS}})^{-3}\\ & + \gamma[-(2qR_{\mathrm{HS}})^4\cos(2qR_{\mathrm{HS}})\\ & + 4[3(2qR_{\mathrm{HS}})^2 - 6]\cos(2qR_{\mathrm{HS}})\\ & + 4[(2qR_{\mathrm{HS}})^3 - 6(2qR_{\mathrm{HS}})]\sin(2qR_{\mathrm{HS}})\\ & + 24](2qR_{\mathrm{HS}})^{-5}\end{aligned}$$

$$\alpha = (1+2\nu)^2/(1-\nu)^4$$

$$\beta = -6\nu(1+\nu/2)^2/(1-\nu)^4$$

$$\gamma = \nu\alpha/2$$

The free variables in this expression are the hard-sphere radius R_{HS} of the randomly packed spherical particles, and the volume fraction ν. The degree of ordering of particles, located at a distance $2R_{\mathrm{HS}}$ from another particle is expressed by ν.

To account for the fact that the relative contributions to scattering of oligomeric and agglomerate-like entities in solution can vary with time, a weighting factor $0 \le \varepsilon \le 1$ is introduced to describe the contribution from the fractal-like structures to the total scattering intensity. The scattering intensity of the sol is then given by

$$\begin{aligned}I(q,t) = {} & N(\Delta\rho)^2 P(q,t)[\varepsilon(t)S_{\mathrm{F}}(q,t)\\ & + (1-\varepsilon(t))S_{\mathrm{C}}(q,t)]\end{aligned} \tag{6}$$

Here N is the number density of spherical particles, and $\Delta\rho$ the scattering contrast between particles and surrounding. The intensity prefactor $\varepsilon N(\Delta\rho)^2$ is associated with the scattering contribution from primary particles that have formed fractal-like structures, and $(1-\varepsilon)N(\Delta\rho)^2$ refers to the remaining agglomerate-like structures with internal correlations that can be described in terms of the structure factor $S_{\mathrm{C}}(q)$.

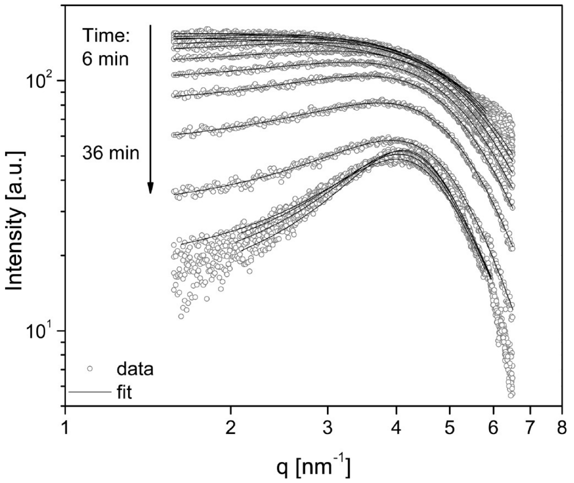

Figure 2. Time-resolved SAXS pattern of drying barium titanate precursor film with h = 0.0 at 60 °C. Data were fitted with the model described by eq 6 assuming a constant value $\varepsilon = 0$.

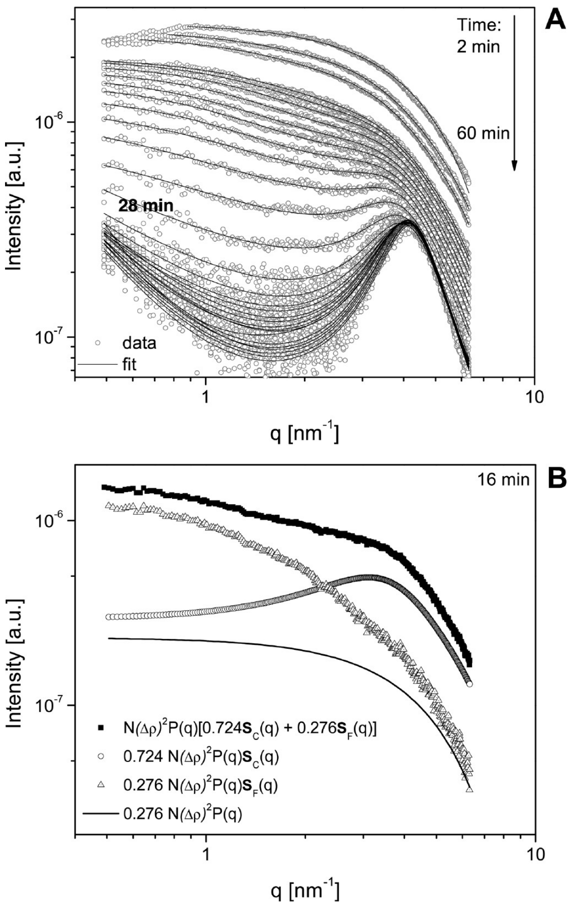

Figure 3. (a) Time-resolved SAXS pattern of drying barium titanate precursor film with h = 5.6 at 60 °C. Data were fitted with the model described by eq 6. (b) Experimental scattering curve (squares) at t = 16 min and separated weighted contributions ($\varepsilon(t)$ = 0.276) of fractal-like particles $P(q)S_F(q)$ (triangles) and $P(q)S_C(q)$ (circles). The simulated scattering curve of a system of noninteracting particles of similar radius r_0 (curve) is shown for the sake of comparison.

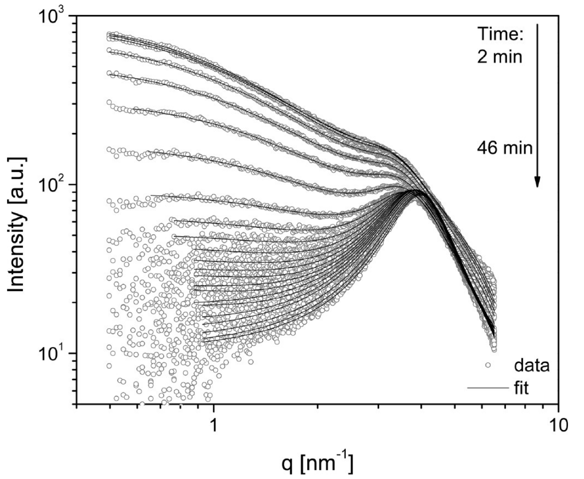

Figure 4. Time-resolved SAXS pattern of drying barium titanate precursor film with h = 33 at 60 °C. Data were fitted with the model described by eq 6.

4. RESULTS AND DISCUSSION

4.1. Time-Resolved SAXS Measurement of Thin Film Drying Process. Figures 2−4 present measured scattering curves of films of BTO model solutions with h = 0, 5.6, and 33.0, together with best fits of eq 6. Due to the fact that all three samples were measured without calibrations of the absolute intensity, the intensities are shown in arbitrary units. Fits of $N(\Delta\rho)^2$ can only be compared within a single measurement series, although differences in trends between different series can be interpreted as well. All $N(\Delta\rho)^2$ values were normalized against a value from the same series at the beginning of the process (i.e., $N(\Delta\rho)^2$ at t = 5 min) .

4.1.1. Drying of Nonhydrolyzed Precursor Sol. Figure 2 displays data of a drying film of a nonhydrolyzed precursor sol of barium titanate, with h = 0. The data set was fitted with eq 6. The evolving system could be described in terms of the spherical form factor and the hard sphere interaction structure factor only, i.e., $\varepsilon = 0$. The factor $N(\Delta\rho)^2$ decreased quickly to *ca.* 7% of its initial value after 28 min (Figure 5A, h = 0). This effect is due to solvent evaporation. The concentration of scattering entities in the film increases as a result of solvent loss during drying. This leads to an increasingly homogeneous film morphology, with accompanying loss of scattering contrast $\Delta\rho$ between scatterers and their surroundings.

The evolution of the primary particles radii r_0 from 0.32 to 0.45 nm is shown in Figure 5B. The evolution of corresponding hard-sphere radii and volume fraction as a function of time is presented in Figure 6, panels A and B. R_{HS} remained practically constant between 0.6 and 0.7 nm. The hard-sphere volume fraction increased from 1.7% to reach 24%, indicating an increasing order in the system during film drying.

4.1.2. Drying of Precursor Sol with h = 5.6. The structural evolution in the film with h = 5.6 upon drying shows a different behavior, as can be seen in Figure 3A. The factor $N(\Delta\rho)^2$ decreased to ca. 20−23% of its initial value after 28 min (Figure 5A, h = 5.6), which is a factor 3 higher than in the unhydrolyzed sol. A slow ongoing evolution in the dried material after 28 min can be recognized in the SAXS patterns in Figure 3. Especially the shift of the broad maximum around q = 3.5 nm^{-1} to higher q values, and the ongoing decrease of scattering intensity in the q-range 1−2 nm^{-1} is well visible in Figure 3A. The size of the primary

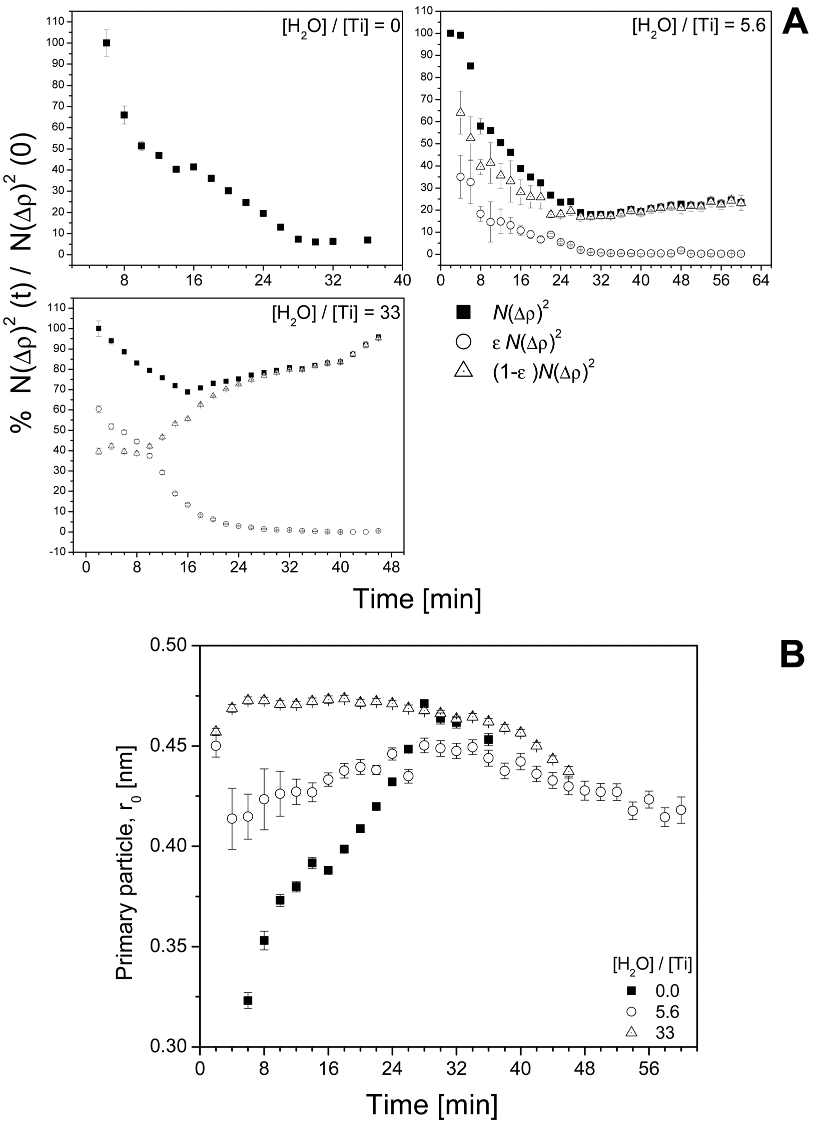

Figure 5. (a) Evolution of $N(\Delta\rho)^2$, contribution from fractal-like structures $\varepsilon N(\Delta\rho)^2$, and contribution from internally correlated structures $(1 - \varepsilon)N(\Delta\rho)^2$. (b) Fitted parameter from spherical form factor $P(q)$: primary particle radius, r_0.

particles varied between 0.41 and 0.45 nm (Figure 5B), very close to values found in the sols under constant volume conditions.[16]

The first scattering curve in the series could be fitted using only the sphere form factor and $S(q) = 1$, i.e., no spatial correlation between particles is present. After 4 min, eq 6 has to be used. Fitted values of $\varepsilon(t)$ are presented in Figure 5A. The fraction $1 - \varepsilon(t)$ related to agglomerates structure factor increased from 65% at $t = 4$ min to >98% at $t = 28$ min. This indicates that the dried film was composed almost exclusively of internally correlated structures. The hard sphere radius and volume faction are presented in Figure 6A and 6B, respectively. R_{HS} decreased slightly from ~0.9 to 0.72 nm. This change is visible in Figure 3 as a shift of the maximum around $q_{max} = 3.5$ nm^{-1} to slightly higher q values. In this case the dimension in real space $d = 2R_{HS} = 2\pi/q_{max}$, which agrees well with the fitted values of all scattering curves. The volume fraction parameter v increased from *ca.* 5% to 30%.

The obtained values of $\varepsilon(t)$ enabled us to estimate the fractions of primary particles that participated in fractal-like agglomerates, and to separate the scattering curves into $P(q)S_F(q)$ and $P(q)S_C(q)$ contributions. Figure 3B presents the experimental scattering curve and the separated contributions $P(q)S_C(q)$ and $P(q)S_F(q)$ at $t = 16$ min. The simulated scattering curve from a system of individual, noninteracting particles of similar radius r_0 is also shown. The increase in the experimental $I(q)$ curve at $q < 4$ nm^{-1} upon decreasing q is caused by the presence of fractal-like structures with gyration radius R_g that are composed of spherical primary particles of radius r_0. Fitting of $P(q)S_F(q)$ yielded the parameters $D = 2.2 \pm 0.2$ and $R_g = 1.13 \pm 0.01$ nm. The number of constituent primary particles n in such a fractal-like structure can be roughly estimated from eq 7, which relates the radius of gyration R_g to n[16,22−24,29] via

$$n = k_0 \left(\frac{R_g}{r_0}\right)^{D} \qquad (7)$$

The value of k_0 can be estimated by assuming an isolated particle, where $n = 1$, as explained in ref 29. For spheres the relationship $R_g = (3/5)^{1/2} r_0$ holds thus, $k_0 = (5/3)^{D/2}$. Since $r_0 = 0.43$ nm, the

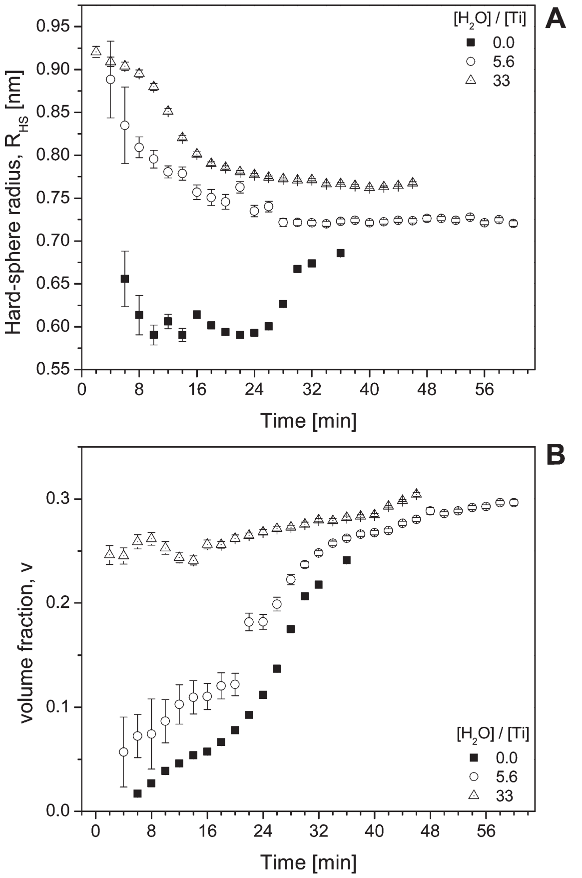

Figure 6. Fitted parameters from correlation structure factor $S_C(q)$: (a) hard-sphere radius $2R_{HS}$. (b) volume fraction, v.

number of particles in the fractal-like agglomerate can be estimated from eq 7, and is equal to approximately 15.

We also fitted the same data with Beaucage's unified exponential/power-law approach[30−32] to compare the values obtained from both fits. In Beaucage's description the Guinier approximation[18] is used to obtain information on different length scales. In our case, two levels are present, namely primary particles of radius of gyration $R_s = (3/5)^{1/2}r_0$, and larger structures of gyration radius R_g. The transition regions between two Guinier regimes are taken into account by error functions that simulate power-law regions. In the present case a two-level fit function, as expressed by eq 8, is required.

$$I(q) = G \exp\left(-\frac{q^2 R_g^{\ 2}}{3}\right) + B \exp\left(-\frac{q^2 R_s^{\ 2}}{3}\right)\left(\frac{[\mathrm{erf}(qR_g 6^{-1/2})]^3}{q}\right)^p + G_s\left(-\frac{q^2 R_s^{\ 2}}{3}\right) + B_s\left(\frac{[\mathrm{erf}(qR_s 6^{-1/2})]^3}{q}\right)^4 \qquad (8)$$

Here G, G_s, and B are constants; p is a scaling exponent of the power law related to R_g; and B_s is constant specific for the description of the limiting q^{-4} Porod region scaling.[17] The following structural parameters were found from the best fit of eq 8 to the experimental data: $R_g = 1.15 \pm 0.04$ nm, $p = 2.06 \pm 0.65$, and $R_s = 0.38 \pm 0.03$ nm. The latter value corresponds to a primary particles radius $r_0 = 0.48 \pm 0.04$ nm. The values obtained by using Beaucage's model are very similar to the ones obtained by using eq 6 as presented in this work. The parameter p in the latter approach is equivalent to D in eq 6, although the error in the fit of p is considerable, because of the short q-range between $q = 2\pi/R_g$ and $2\pi/R_s$. It can be concluded that Beaucage's structural model supports our findings based on eq 6. When we used eq 8 to fit the other experimental data, we obtained the same values of R_g as with eq 6 within only 3% error margin.

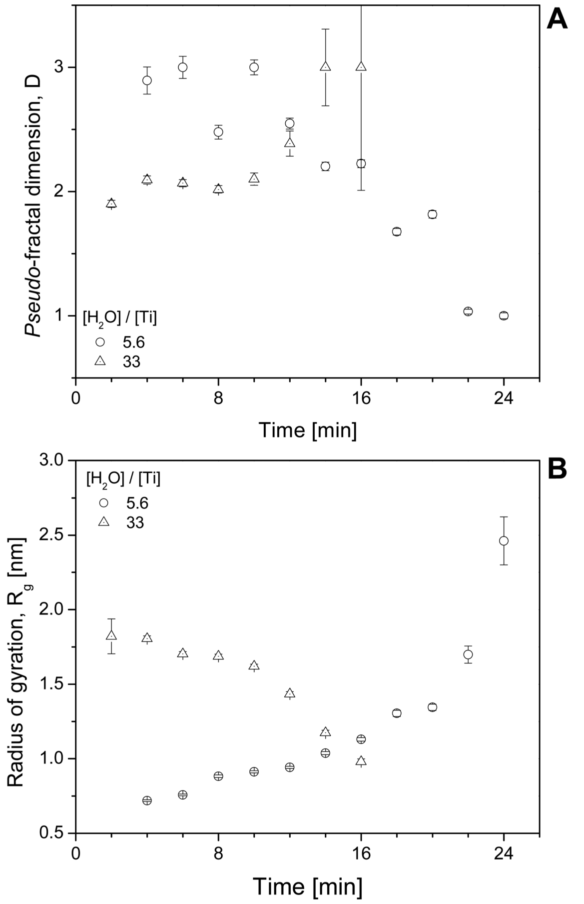

Figure 7. Fitted parameters from mass-fractal structure factor $S_F(q)$: (a) pseudofractal dimension D and (b) radius of gyration, R_g.

The best fits of D and R_g from eq 6 are presented in Figure 7. In the first 24 min of the drying process, when the film was still wet, small fractal-like structures were present along with a majority of internally correlated structures (Figure 5A). After this, the contribution from fractal structures was too small to be fitted. The fractal-like structures remained relatively small ($R_g \approx 1$ nm) until $t = 20$ min. The D parameter was relatively high (>2), indicating that the small clusters were relatively compact. Just before the film became dry at $t = 22$ min, a relatively rapid growth of R_g started, which was accompanied by a decrease of D, probably indicating a rapid agglomeration process.

4.1.3. Drying of Precursor Sol with h = 33.0. The time-resolved scattering curves of a drying BTO precursor film with $h = 33$ is shown in Figure 4. The normalized factor $N(\Delta\rho)^2$ decreased slowly in the first 16 min to 70% of its original value, and then increased to >90% (Figure 5A). The factor $1 - \varepsilon(t)$, associated with the contribution of internally correlated structures to the total scattering intensity, increased from ca. 40% at $t = 2$ min to

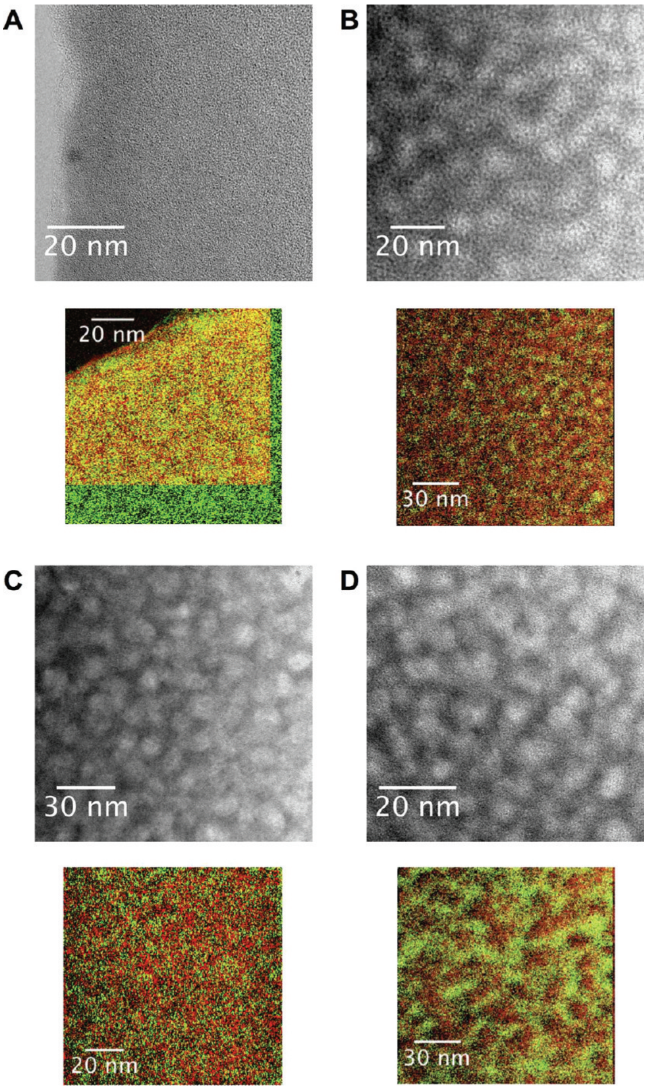

Figure 8. Bright-field TEM images (upper figure) and EELS mappings of Ba (red) and Ti (green) (lower figure) of as-dried BTO films with varying h; (a) h = 0.0, (b) 2.8, (c) 5.6, and (d) 33.

>99% after t = 22 min. The contribution of fractal-like structures was considerable in the first 10 min, and then decreased quickly to almost zero. Drying increases the concentration of precursors, thereby shortening the gelation time. Highly hydrolyzed sols are known to undergo sol−gel transition relatively quickly at 60 °C.[16] Therefore, a chemical gel was formed in a shorter period of time with respect to the film hydrolyzed with h = 5.6. The size of the primary particles r_0 remained constant at 0.42−0.47 nm throughout the process (Figure 5B). R_{HS} in Figure 6A decreased from initial 0.92 nm radius to a constant value of 0.77 nm after t = 24 min. The volume fraction parameter, v was higher than in the other two sols.

The initial R_g values (Figure 7B) were higher than in the film with h = 5.6, but they decreased to similar values at t = 12 min. The parameter D increased from 1.9 to 2.4 in the same time interval (Figure 7A). The actual change of gyration radius by almost a factor of 2 was therefore considerable. In view of the minor change of D within experimental error, the morphology of the fractal-like structures became slightly more densely packed. Values of R_g and D after t = 12 min were 1.0 nm and 3, respectively, indicating the formation of small and fully dense agglomerates. It is noted that since the contribution of fractal-like structures to $N(\Delta\rho)^2$ was only ~10% of the total, the errors here were larger because of the relatively low signal-to-noise ratios.

4.2. EELS and TEM Characterization. EELS analysis yielded two-dimensional qualitative maps of the distribution of Ba and Ti elements in as-dried, not annealed films. Figures 8 shows TEM and corresponding EELS elemental mappings of Ba and Ti in films from sols with h = 0.0, 2.8, 5.6, and 33. The film thicknesses were practically constant in the characterized areas.

The film prepared from a sol with h = 0 showed a very homogeneous morphology. EELS mapping showed that Ba- and Ti-rich areas were small (1−2 nm) and homogenously distributed in the film, indicating good mixing of Ba and Ti species on molecular level. In contrast, the bright-field TEM image of a film with h = 2.8 in Figure 8B indicated formation of quasi-spherical interconnected domains of 1 nm diameter, which had agglomerated into larger objects of 5−10 nm size (Figure 8B). These features appeared brighter, indicating that their electron density was lower than in the surrounding darker regions. The darker areas did not exhibit a particulate shape and were 5−10 nm in diameter. The morphology resembles the morphology found in the film with h = 5.6 (Figure 8C). The corresponding EELS mappings showed that the dark regions in the TEM images correspond to Ba-rich regions, and the bright regions to a Ti-rich phase. The Ba- and Ti-rich domains were separated over an average distance of 5−10 nm. The Ti-rich phase appears slightly smaller, with a correlation length of ca. 3 nm, in the film with lower h.

When h was increased to 33, the film showed a bright particle-like structure with diameters of 5−10 nm in a bright-field TEM image (Figure 8D). The EELS mapping showed that the Ba- and Ti-rich regions were separated on a length-scale of 15−20 nm. The Ti-rich areas seem to be isolated from other Ti-rich regions (in a 2D image), and they were of higher Ti density than in films with lower h. These results clearly demonstrate that the spatial separation of Ba and Ti in the film is dependent on the extent of hydrolysis of the precursor sols. It is noted that the bright-field TEM images of the three hydrolyzed sols did not show significant differences in morphology. The EELS mapping revealed more details of the structure of the film.

4.3. Interpretation of SAXS and EELS Data. In a previous study on the structural evolution of BTO precursors sols at a constant volume of solvent,[16] we found that the sol−gel process consists of three phases: (i) formation of primary scatterers with r_0 = 0.45 nm and very small agglomerates; (ii) growth of fractal-like structures and structures with internal spatial correlations, which were attributed to branched polymer-like Ti-based oligomers and agglomerates of similarly sized particles (R_{HS} = 0.90−0.95 nm), respectively; and (iii) gelation as a result of cluster−cluster aggregation of the fractal-like structures.

In the current study on physically drying films with similar composition we found several analogies with our previous findings.[16] The primary scatterers were spherical and had a radius r_0 of 0.32−0.47 nm, depending on the value of h, and the stage of the drying process. Typical values were ~0.45 nm, which is the same as found in the previous study. Similar structural motifs have been observed by SAXS in a number of titania-related gelling systems,[33−37] suggesting that the scatterers in the present study were similarly composed of titania. It is noted that the value of r_0 hardly varied in the hydrolyzed films in the course of the drying process, while it increased in the first 24 min of drying of a

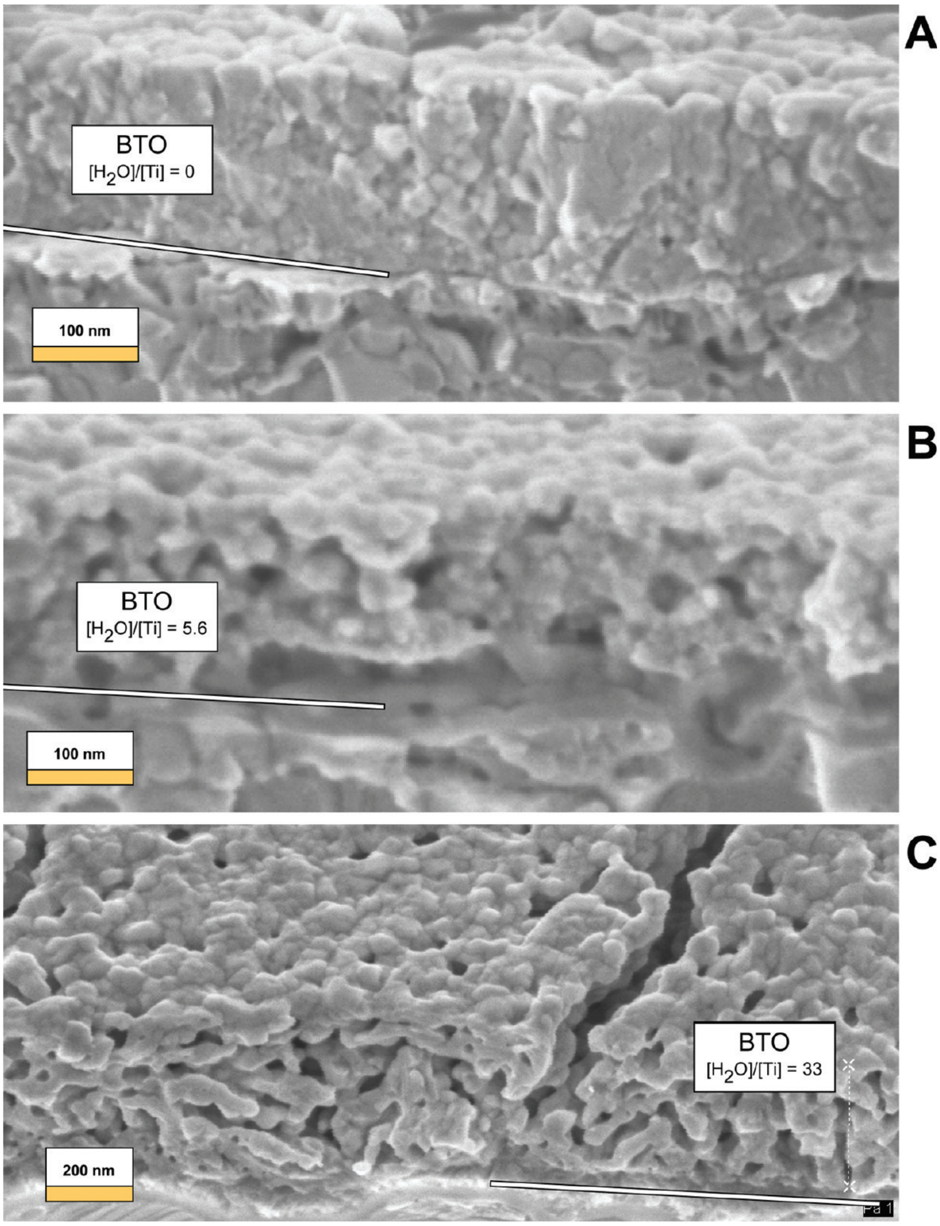

Figure 9. HR-SEM images of the cross sections of BTO films crystallized at 700 °C with varying h; (a) h = 0.0, (b) 5.6 and (c) 33.

nonhydrolyzed film. Apparently, the primary scatterers require the presence of water to grow to a size of 0.42−0.47 nm. The nonhydrolyzed film probably either absorbed moisture from air or was hydrolyzed due to the esterification reaction between solvent alcohol and acetic acid. By the end of the drying process the primary scatterers in all three investigated films appear to have the same size within experimental error, independent of the initial value of h.

The hard sphere radius R_{HS} in the structures with internal correlations (Figure 6) is larger than r_0. This suggests that the Ti-based core of size r_0 was probably surrounded by a stable ligand shell containing oxo, hydroxy, alkoxy and/or acetate groups. Since the electron density in the ligand shell is virtually identical to the density of the surrounding solvent matrix, it cannot be detected directly by SAXS. However, the average distance between primary scatterers in agglomerates with internal correlations is directly dependent on the thickness of the ligand shell, so they are included in R_{HS}.[16] The values of R_{HS} in different films were relatively similar, from 0.7−0.9 nm. Lower values were measured in the nonhydrolyzed film. In the hydrolyzed sols, the initial value was 0.9 nm and it decreased gradually to ∼0.75 nm. In the nonhydrolyzed films the trend was opposite, and it followed the same increasing trend as r_0. This suggests that in all cases, very similar species form at the primary structural level, with an inorganic core of ∼0.45 nm radius and a ligand shell of ∼0.3 nm thickness in the as-dried film. Since the hard sphere radius R_{HS} was ∼0.9 nm, with an inorganic core of radius $r_0 \approx 0.45$ nm in hydrolyzed BTO sols,[16] it seems that drying does not affect the radius of the inorganic core, but the thickness of the outer organic ligand shell shrinks by ∼0.15 nm.

The increase of volume fraction ν upon drying shows the increasing packing density in as-dried films. Its initial value was close to zero for the nonhydrolyzed film, and ν = 0.25 for the film with $h = 33$, but it evolved to very similar values of $\nu \approx 0.3$ in all investigated systems. In hydrolyzed BTO sols at a constant solvent volume,[16] the final packing density was slightly higher ($\nu = 0.4$) than found in the present work. The same study showed that gelation occurs via aggregation of fractal-like branched oligomers, while the contribution of internally correlated structures to the total scattering intensity decreased during the course of the reaction. In contrast, in physically drying thin films, the contribution from fractal-like structures to scattering diminished in the course of drying. Moreover, their gyration radius remained much smaller than in sols with constant solvent volume. Apparently, the disappearance of fractal-like structures is associated with the loss of solvent from the sol. The fractal-like structures are probably not stable in the absence of a stabilizing solvent phase.

Very strong correlation peaks developed in nearly dry films, indicating that the as-dried film consisted entirely of agglomerates with correlated hard-sphere interactions, e.g., random close-packed agglomerates composed of similarly sized nanoparticles.

The overall trends in $\varepsilon(t)$ and $N(\Delta\rho)^2$ in Figure 5A can be explained in terms of the occurrence of condensation (up to gelation) and physical evaporation of solvents from the film. Since the evolved nanostructures visible with SAXS are most likely entirely Ti-based,[16] they influence the value of $\varepsilon(t)$ and $\Delta\rho$. On the other hand, the Ba ions remain dissolved in the acetic acid matrix and mainly influence the scattering contrast between nanostructure and solvent $\Delta\rho$. Ba^{2+} ions precipitate when their concentration exceeds the actual solubility limit of the system, for instance as a result of loss of acetic acid from the film. The gradual decrease of $N(\Delta\rho)^2$ in Figure 5A in the first period of drying can be interpreted in terms of the mutual approach of Ti-based nanostructures upon solvent loss, which results in an effective decrease of $\Delta\rho$ between these nanostructures and their surroundings. However, the reversal in the trend of $N(\Delta\rho)^2$ in the hydrolyzed films after 16−24 min of drying suggests that the $\Delta\rho$ increases in the last stages of drying, and/or that N increases. The most plausible explanation for that phenomenon is that a Ba-rich phase precipitates from solution. The effect is particularly pronounced for the film with $h = 33$, which also shows the most pronounced degree of separation between Ti-rich and Ba-rich domains in the as-dried film (Figure 8D). Our data showed that the Ti-based structures in solution are larger at higher water concentrations. It is well possible that the size of these structures is one of the main factors that determine the length scale on which phase separation of Ba- and Ti-rich domains occurs.

4.4. Microstructure of Crystalline Films. The presence of hydrolysis-modulated inhomogeneities in the precursor thin films was anticipated to have an effect on the microstructure of crystalline $BaTiO_3$ films. BTO precursor films were therefore deposited onto Si/Ti/Pt wafers and crystallized at 700 °C for 15 min by rapid thermal annealing. The cross sections of films obtained from BTO precursor sols with $h = 0.0$, 5.6, and 33 are presented in Figure 9. XRD analysis (not shown here) confirmed that phase pure barium titanate films were obtained in all three cases. However, very different microstructures were obtained. The film synthesized from a water-free BTO sol (Figure 9A) was composed of spherical grains of ca. 20 nm diameter, and exhibited the lowest porosity of all three films. For films with $h = 5.6$ (Figure 9B) the porosity of the film was larger. The film synthesized from a sol with $h = 33$ was even more porous, and consisted of grains of 50−100 nm diameter (Figure 9C). Visible cracks were present. We attribute the observed differences in the final microstructure to the initial composition variation in the as-dried films. The increasing spatial separation between Ba-rich and Ti-rich areas led to longer diffusion lengths upon crystallization of $BaTiO_3$ from the amorphous xero-gel and caused an increase in porosity of the film.

5. CONCLUSIONS

The structures in solution that are visible with SAXS are Ti-rich, and can be divided into fractal-like branched oligomers, and dense agglomerates of similarly sized nanoparticles. A model was developed to describe the scattering behavior of these solutions in terms of these nanostructures, and this model was able to fit the experimental data well over a wide range of conditions. Both types of structures consist of the same type of primary scatterers, namely particles with an inorganic core of ∼0.45 nm radius, and an outer organic shell of ∼0.3 nm thickness in the as-dried films. The shell was ∼0.15 nm thicker in the initial sols, and probably shrunk in the course of drying. The fractal-like morphologies disappeared during film drying, most likely because they were not stable in the absence of a solvent matrix. Only the agglomerate-like structures remained in the as-dried films. In general, the trends visible in Figure 5−7 are similar for films with different values of h, especially after longer periods of time.

EELS showed that phase separation between barium and titanium-rich domains had occurred after the drying of these films. Their morphology looked similar in TEM analyses, but EELS showed considerable differences between films, because the distribution of Ba and Ti varied strongly depending on the hydrolysis conditions. Nonhydrolyzed sols yielded a homogeneous distribution of elements, whereas high hydrolysis ratios promoted separation of Ba- and Ti-rich domains with a correlation length of *ca.* 15 nm. This demonstrates that such as-dried films are not necessarily uniform on the mesoscopic level. The inhomogeneity influenced the microstructure of thermally processed crystalline BTO films and caused increasing porosity with increasing hydrolysis ratio.

■ AUTHOR INFORMATION

Corresponding Author

*E-mail: j.e.tenelshof@utwente.nl.

■ ACKNOWLEDGMENT

This work was financially supported by The Netherlands Technology Foundation STW. We thank The Netherlands Organization for Scientific Research (NWO) for providing us with beam time at the ESRF DUBBLE-BM26B beamline. Beamline staff of DUBBLE is thanked for their competent support.

■ REFERENCES

(1) Yoon, D. *J. Ceram. Proc. Res.* **2006**, *7*, 343–354.
(2) Schwartz, R. W.; Schneller, T. S.; Waser, R. *C.R. Chim.* **2004**, *7*, 433–461.
(3) Pithan, C.; Hennings, D. H.; Waser, R. *Int. J. Appl. Ceram. Technol.* **2005**, *2*, 1–14.
(4) Schwartz, R. W.; Narayanan, M. Chemical Solution Deposition —Basic Principles. In *Solution Processing of Inorganic Materials*; Mitzi, D. B., Ed.; John Wiley & Sons, Inc.: New York, 2009; pp 33−76.
(5) Huffman, M. *Integr. Ferroelectr.* **1995**, *10*, 39–53.
(6) Phule, P. P.; Risbud, S. H. *Adv. Ceram. Mater.* **1988**, *3*, 183–185.
(7) Assink, R. A.; Schwartz, R. W. *Chem. Mater.* **1993**, *5*, 511–517.

(8) Hasenkox, U.; Hoffmann, S.; Waser, R. *J. Sol-Gel Sci. Technol.* **1995**, *12*, 67–79.

(9) Hoffmann, S.; Waser, R. *J. Eur. Ceram. Soc.* **1999**, *19*, 1339–1343.

(10) Frey, M. H.; Payne, D. A. *Chem. Mater.* **1995**, *7*, 123–129.

(11) Hennings, D.; Rosenstein, G.; Schreinemacher, H. *J. Eur. Ceram. Soc.* **1991**, *8*, 107–115.

(12) Zhang, Q.; Huang, Z.; Vickers, M. E.; Whatmore, R. W. *J. Europ. Ceram. Soc.* **1999**, *19*, 1417–1421.

(13) Zhang, Q.; Vickers, M. E.; Patel, A.; Whatmore, R. W. *J. Sol-Gel Sci. Technol.* **1998**, *11*, 141–152.

(14) Zhang, Q.; Whatmore, R. W.; Vickers, M. E. *J. Sol-Gel Sci. Technol.* **1999**, *15*, 13–22.

(15) Stawski, T. M.; Besselink, R.; Veldhuis, S. A.; Castricum, H. L.; Blank, D. H. A.; Ten Elshof, J. E. *J. Colloid Interface Sci.*; DOI: 10.1016/j.jcis.2011.12.033.

(16) Stawski, T. M.; Veldhuis, S. A.; Besselink, R.; Castricum, H. L.; Portale, G.; Blank, D. H. A.; ten Elshof, J. E. *J. Phys. Chem. C* **2011**, *115*, 20449–20459. Stawski, T. M.; Veldhuis, S. A.; Besselink, R.; Castricum, H. L.; Portale, G.; Blank, D. H. A.; ten Elshof, J. E. *J. Phys. Chem. C* **2011**, *115*, 24028–24028.

(17) Guinier, A.; Fournet, G. *Small Angle Scattering of X-rays*; John Wiley & Sons Inc, New York, 1955.

(18) Kratky, O. A Survey. In *Small Angle X-ray Scattering*; Ed. Glatter, O.; Kratky, O. Academic Press, London, 3—13, 1982.

(19) Porod, G. General theory. In *Small Angle X-ray Scattering*; Glatter, O., Kratky, O., Eds.; Academic Press, London, 17—52, 1982.

(20) Craievich, A. F. *Mater. Res.* **2002**, *5*, 1–11.

(21) Bras, W.; Dolbnya, I. P.; Detollenaere, D.; van Tol, R.; Malfois, M.; Greaves, G. N.; Ryan, A. J.; Heeley, E. *J. Appl. Crystallogr.* **2003**, *36*, 791–794.

(22) Teixeira, J. *J. Appl. Crystallogr.* **1988**, *21*, 781–785.

(23) Freltoft, T.; Kjems, J. K.; Sinha, S. K. *Phys. Rev. B* **1986**, *33*, 269–275.

(24) Berry, M. V.; Percival, I. C. *Opt. Acta* **1986**, *33*, 577–591.

(25) Percus, J. K.; Yevick, G. J. *Phys. Rev.* **1958**, *110*, 1–13.

(26) Vrij, A. *J. Chem. Phys.* **1979**, *71*, 3267–3270.

(27) Baxter, R. J. *J. Chem. Phys.* **1968**, *49*, 2770–2774.

(28) Kinning, D. J.; Thomas, E. L. *Macromolecules* **1984**, *17*, 1712–1718.

(29) Sorensen, C. M. *Aerosol Sci. Technol.* **2001**, *35*, 648–687.

(30) Beaucage, G. *J. Appl. Crystallogr.* **1995**, *28*, 717–728.

(31) Beaucage, G. *J. Appl. Crystallogr.* **1996**, *29*, 134–146.

(32) Beaucage, G.; Ulibarri, T. A.; Black, E. P.; Schaefer, D. W. Multiple Size Scale Structures in Silica-Siloxane Composites Studied by Small-Angle Scattering. In *Hybrid Organic-Inorganic Composites*; ACS Symposium Series; Mark, J. E., Lee, C. Y-C., Bianconi, P. A., Eds.; American Chemical Society: Washington DC, 1995.

(33) Doeuff, S.; Henry, M.; Sanchez, C. *Mater. Res. Bull.* **1990**, *25*, 1519–1529.

(34) Jalava, J. - H.; Hiltunen, E.; Kähkönen, H.; Erkkilä, H.; Härmä, H.; Taavitsainen, V.-M. *Ind. Eng. Chem. Res.* **2000**, *39*, 349–361.

(35) Torma, V.; Peterlik, H.; Bauer, U.; Rupp, W.; Husing, N.; Bernstorff, S.; Steinhart, M.; Goerigk, G.; Schubert, U. *Chem. Mater.* **2005**, *17*, 3146–3153.

(36) Pattier, B.; Henderson, M.; Brotons, G.; Gibaud, A. *J. Phys. Chem. B* **2010**, *114*, 5227–5232.

(37) Kessler, V. G. *J. Sol-Gel Sci. Technol.* **2009**, *51*, 264–271.